PCCP

PAPER

View Article Online
View Journal | View Issue

Check for updates

Cite this: *Phys. Chem. Chem. Phys.*, 2022, **24**, 10210

An analysis of Schottky barrier in silicene/Ga_2SeS heterostructures by employing electric field and strain†

R. Caglayan,[a] H. E. Guler[a] and Y. Mogulkoc *[b]

Received 14th January 2022,
Accepted 1st April 2022

DOI: 10.1039/d2cp00228k

rsc.li/pccp

Two-dimensional materials are leading the way in nanodevice applications thanks to their various advantages. Although two-dimensional materials show promise for many applications, they have certain limitations. In the last decade, the increasing demand for the applications of novel two-dimensional materials has accelerated heterostructure studies in this field. Hence, restoring the combination of two-dimensional heterostructured materials has been reported. In this paper, we show that the effect of the external electric field and biaxial strain on the silicene/Ga_2SeS heterostructure has a critical impact on the tuning of the Schottky barrier height. The findings such as the variation of the electronic band gap, interlayer charge transfer, total dipole moment, and n-type/p-type Schottky barrier transitions of the silicene/Ga_2SeS heterostructure under external effects imply that the device performance can be adjusted with Janus 2D materials.

Published on 05 April 2022. Downloaded by Ankara University on 10/29/2022 10:51:31 AM.

I Introduction

Janus two-dimensional (2D) materials are constructed by breaking the out-of-plane symmetry of the parent material. The broken symmetry reveals the exceptional electronic and optical properties of materials. Therefore, Janus 2D materials are considered as promising candidates for many applications such as photovoltaics,[1–4] photocatalysis,[5–7] gas sensors,[8–10] batteries, and so on. Since Janus 2D materials do not exist in nature, the preparation procedure is still challenging due to their limited material quality and thermodynamic instability.[11] Nevertheless, 2D Janus MoSSe and WSSe which are considered pioneering Janus materials have been studied experimentally with different approaches.[12–14]

In the last decade, group III dichalcogenides also known as MX-type (M = Ga, In; X = S, Se, Te) materials have been studied extensively in the literature.[15–19] It has been demonstrated that these materials are suitable for optoelectronic applications due to their indirect band gaps[19,20] and high photoresponsivity.[21] Moreover, breaking the out-of-plane symmetry of group-III dichalcogenides' structure can enhance the physical properties compared to the constituent material. Therefore, recently novel Janus group-III dichalcogenides materials have been proposed.[22–25] The study of novel Janus group-III materials by combining them with different 2D graphene-like structures began to be studied after such studies.

Silicene, which has been successfully synthesized by using various substrates and approaches,[26–30] is a silicon analog of graphene that has low buckling and massless Dirac-fermion charge carriers, having a band structure similar to that of graphene.[31] The buckling in silicene occurs due to the pseudo-Jahn–Teller distortion, which results in the mixed sp^2–sp^3 hybridization. Also, the buckling provides not only stability but also freedom in adjusting the electronic properties of silicene.[32,33]

The formation of vdW heterostructures is one of the prominent methods for effectively tuning the electronic properties of 2D materials. For this reason, vdW heterostructures of 2D materials are widely used for applications that can be easily integrated into nanoscale materials.[34–38] In particular, with the formation of metal/semiconductor vdW heterostructures, a phenomenon called Schottky barrier emerges. The Schottky barrier is crucial because it has a critical effect on device performance, *e.g.*, the Schottky barrier is strongly affected by the absorption of chemical and biological species.[39] Hence, this has given rise to the idea that Schottky contacts can be used as gas sensors. From this, Quang *et al.*[40] have shown that a graphene/SnO_2 Schottky contact-based gas sensor displays a low operating temperature of 150 °C with an enhanced response/recovery time. Further, Kwon *et al.*[41] have revealed that the carrier mobility of MoS_2 increased with the lowering of Schottky barrier height (SBH). Moreover, He *et al.*[42] studied the characteristics of the vertical and lateral interfaces

[a] *Department of Physics, Faculty of Science, Ankara University, 06100, Ankara, Turkey*
[b] *Department of Physics Engineering, Faculty of Engineering, Ankara University, 06100, Ankara, Turkey. E-mail: mogulkoc@eng.ankara.edu.tr*

† Electronic supplementary information (ESI) available. See DOI: https://doi.org/10.1039/d2cp00228k

This journal is © the Owner Societies 2022

Published on 05 April 2022. Downloaded by Ankara University on 10/29/2022 10:51:31 AM.

between monolayer SnSe and metals which represent the electrode selection for monolayer SnSe based FET devices.

Accordingly, to improve the device performance of 2D metal/semiconductor vdW materials, it is essential to modify the SBH. The SBH can be adjusted by utilizing external stimuli such as an external electric field and strain.[43–47] In addition, it has been shown by Le *et al.*[48] that an n-type Schottky contact is formed with a small SBH in the silicene/GaSe heterostructure. It raises the question of whether the SBH can be modified using the Janus counterpart of the corresponding material. In accordance with this question, we investigate the effect of the intrinsic electric field of Ga_2SeS on the Schottky barrier height in this study. Moreover, we examine the electronic properties of the silicene/Ga_2SeS heterostructure under electric field and strain to gain deep insight into the tunable Schottky barrier for Janus 2D materials. We analyze the strain and electric field effects on this heterostructure through the determination of SBH and interlayer charge transfer, and observe that the SBH changed from n-type to p-type or an ohmic contact. As a result, we conclude that the SBH of Janus Ga_2SeS is highly sensitive to external effects and that changing the magnitudes of the electric field and strain can improve the device performance.

II Method

The first principles calculations based on density functional theory (DFT) were performed using the projected augmented wave (PAW) method[49] implemented in the Vienna *ab initio* simulation package (VASP).[50–53] The generalized gradient approximation (GGA) formulated by Perdew–Burke–Ernzerhof (PBE)[54] was taken as the exchange–correlation functional. To obtain a more accurate energy band gap, a Heyd–Scuseria–Ernzerhof (HSE06)[55,56] screened hybrid functional was applied on top of the DFT-PBE. The plane wave cut-off energy was set to 800 eV. The Brillouin zone (BZ) integration was performed using the gamma-centered Monkhorst–Pack method[57] with a 16 × 16 × 1 *k*-point mesh. To describe the effect of vdW interactions between two layers, the DFT-D2 method[58] was employed. To optimize the atomic positions and lattice constant, the conjugate gradient method was used. In the geometrical optimization, the maximum Hellmann–Feynman force acting on each atom is less than 0.05 eV $Å^{-1}$. The energy convergence criterion between two sequential steps was taken to be 10^{-8} eV. The vacuum spacing along the *z*-direction to prevent interactions between adjacent layers was employed as 25 Å. The Bader charge analysis developed by Henkelman *et al.*[59–61] was performed to investigate the charge transfer between two layers. The phonon spectrum was determined by using the PHONOPY[62] code based on density functional perturbation theory (DFPT) with employing a 4 × 4 × 1 supercell approximation. The thermodynamic stability of the silicene/Ga_2SeS heterostructure was further investigated by using *ab initio* molecular dynamics (AIMD) simulations. The system has been regarded as a canonical ensemble, with a 4 × 4 × 1 supercell and the Andersen thermostat. The temperature was set to 300 K within a total simulation time of 4 fs in a 1 fs time interval.

Further, to gain insight into the rate of migration of electrons and holes, the carrier mobility has been examined by utilizing deformation potential theory (DPT) formulated by Bardeen and Shockley:[63]

$$\mu = \frac{e\hbar^3 C_{2D}}{k_B T m^* m_d E_1^2} \quad (1)$$

where e, $\hbar$, k_B, and T are the electric charge, reduced Planck constant, Boltzmann constant, and temperature, respectively. m^* is the effective mass along the transport direction and defined by the formula: $m^* = \hbar^2 [\partial^2 E/\partial^2 k]^{-1}$ and $m_d = (m_x m_y)^{1/2}$ is the average effective mass. E_1 is the deformation potential and is defined by the formula: $E_1 = E_{edge}/(\delta\varepsilon)$, where E_{edge} represents the energy shifting of the conduction band minimum and valence band maximum in the presence of strain. C_{2D} denotes the in-plane stiffness and is defined by the formula: $C_{2D} = 2[\partial^2 E_{tot}/\partial\varepsilon^2]/S_0$, where E_{tot} is the total energy and S_0 is the total area of the unit cell.

III Results and discussion

A Structural analysis and electronic properties of the pristine heterostructure

We first perform the structural optimization of pristine silicene and Ga_2SeS monolayers. The lattice parameters of silicene and Ga_2SeS are 3.87 Å and 3.73 Å, respectively, which are compatible with previous studies.[25,64,65] We also calculated the cohesive energy (E_{coh}), which is a crucial parameter indicating the synthesis feasibility of monolayer Ga_2SeS.[66] The cohesive energy is calculated by using the formula: $E_{coh} = [n_{Ga}E_{Ga} + n_{Se}E_{Se} + n_S E_S - E_{Ga_2SeS}]/n_{tot}$, where E_{Ga_2SeS} is the total energy of the system E_{Se} and E_S are the single atom energies of Se and S atoms, respectively. n_{Ga}, n_{Se}, and n_S are the numbers of Ga, Se, and S atoms, respectively, and n_{tot} is the total number of atoms in the unit cell. We first calculated the E_{coh} for freestanding GaS and GaSe and found them to be 2.882 and 2.340 eV per atom, respectively, which are compatible with previous reports.[19] After that, we have found that the E_{coh} value of Ga_2SeS is 2.591 eV, which is between the values of the binary counterparts. This cohesive energy is relatively high, which indicates that the atoms in the system are tightly bonded, and thus it can be concluded that it is suitable for synthesis. The lattice mismatch between the silicene and Ga_2SeS is approximately 3.62%, which is significant. However, the buckling of silicene compensates for the intrinsic strain created by the lattice mismatch. To evaluate the most convenient configuration for the formation of the heterostructure, we consider six different stacking patterns, called AA1, AA2, AB1, AB2, AB3, and AB4, as presented in Fig. 1. To guarantee the most stable and favorable structure among all six stacking patterns the binding energies need to be addressed.[67] We, therefore, calculate the binding energies of the stacking patterns which is expressed by $E_b = E_{silicene/Ga_2SeS} - E_{silicene} - E_{Ga_2SeS}$ where $E_{silicene/Ga_2SeS}$, $E_{silicene}$, and E_{Ga_2SeS} represent the total energies of the structures. All stacking patterns are negative proving the structural stability,

Published on 05 April 2022. Downloaded by Ankara University on 10/29/2022 10:51:31 AM.

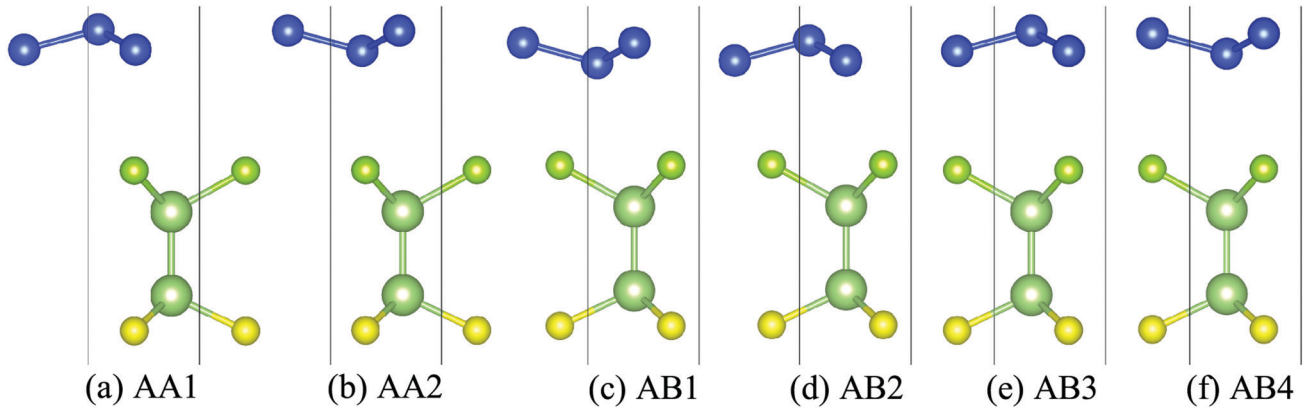


Fig. 1 The possible stacking patterns of silicene/Ga_2SeS vdW heterostructures: (a) AA1, (b) AA2, (c) AB1, (d) AB2, (e) AB3, and (f) AB4.

yet the AB1 stack has the lowest binding energy among all stacking patterns whose binding energies are listed in Table 1. The illustration of the optimized silicene/Ga_2SeS heterostructure is shown in Fig. 2(a). The lattice parameter of the silicene/Ga_2SeS heterostructure is 3.75 Å, which is in the acceptable range. We determine the dynamic stability of the system by investigating the phonon spectrum. As shown in Fig. 2(b), all phonon branches are positive, indicating that the structure is stable. Also, we examine the thermodynamic stability of the silicene/Ga_2SeS heterostructure *via* AIMD simulations at room temperature (300 K). In Fig. 3, the energy fluctuation and snapshots of the system at 4 ps total simulation are depicted. From Fig. 3(a)–(d), we notice that the energy fluctuations are considerably small, and there is no structural deformation during the total simulation time. In addition, as shown in Table 2, the bond length of Si–Si (d_{Si-Si}) decreases, while the bond lengths of Ga–S (d_{Ga-S}) and Ga–Se (d_{Ga-Se}) increase with the formation of the heterostructure.

The electronic band structures of silicene and Ga_2SeS monolayers are presented in Fig. 4. As also given in Table 2, silicene is a semi-metal, and Ga_2SeS is an indirect semiconductor with a band gap value of 2.02 eV (3.18 eV) for PBE (HSE06) approximation. The silicene/Ga_2SeS heterostructure shows direct semiconducting behavior with a 0.18 eV (0.22 eV) band gap value for PBE (HSE06) (see Fig. 2(c)). The HSE06 method, as expected, increases the band gap by lifting the conduction band minimum (CBM) in both pristine and heterostructure electronic band structures.

In order to describe precisely the interlayer charge transfer mechanism of silicene/Ga_2SeS heterostructures, we take into account charge densities, electrostatic potential, and dipole moments. In Fig. 5(a), we plot the plane-averaged charge density difference along the z-direction by using the formula:

$$\Delta\rho(z) = \rho_{\text{silicene/Ga}_2\text{SeS}} - \rho_{\text{silicene}} - \rho_{\text{Ga}_2\text{SeS}} \quad (2)$$

where $\rho_{\text{silicene/Ga}_2\text{SeS}}$, ρ_{silicene}, and $\rho_{\text{Ga}_2\text{SeS}}$ denote the plane-averaged charge density values of silicene/Ga_2SeS, silicene and Ga_2SeS, respectively. The charge is accumulated in Ga_2SeS and depleted in the silicene region, as shown in the plane-averaged charge density (in Fig. 5(a)). In addition, we found that the charge is transferred from silicene to Ga_2SeS with a value of 0.03 $|e|$ by Bader charge analysis, which is consistent with the plane-averaged charge density difference. We depict in Fig. 5(b) the plane-averaged electrostatic potential along the z-direction. The electrostatic potentials of S and Se differ from each other, implying the Janus behavior of Ga_2SeS. Also, S has a deeper potential than Se. This is because S (2.5) has a slightly higher electronegativity than Se (2.4). In the heterostructure case, the potential drop across the interface is 8.7 eV, which induces a strong electric field. The dipole moment, which shows the presence of an intrinsic electric field in the Janus Ga_2SeS monolayer, was found to be −0.016 eÅ (−0.077 Debye).[68] The negative sign denotes that the intrinsic electric field is directed from Se to S. Likewise, the silicene/Ga_2SeS heterostructure has a dipole moment correlated to the interlayer charge transfer and the intrinsic electric field. For the silicene/Ga_2SeS heterostructure, the total dipole moment is in the same direction as the interlayer charge transfer. Nevertheless, the intrinsic dipole moment of the monolayer Ga_2SeS strengthens the total dipole moment of the silicene/Ga_2SeS heterostructure (see Table 2).

Moreover, in Fig. 6, we present the layer-dependent projected electronic band structure and the band alignment of the silicene/Ga_2SeS heterostructure. The silicene layer contributes to both the CBM and VBM, as shown in Fig. 6(a). These results are in agreement with the highest occupied molecular orbitals (HOMOs) (valence band) and lowest unoccupied molecular orbitals (LUMOs) (conduction band) that we show in Fig. 5(c) and (d). The band edges of silicene/Ga_2SeS heterostructures are shown in Fig. 6(a), where the band alignments are set to the energy of a stable electron within the vacuum level. The work function of the

Table 1 Binding energies of silicene/Ga_2SeS heterostructures for the AA1, AA2, AB1, AB2, AB3, and AB4 stacking patterns

Pattern	Binding energy (eV)
AA1	−0.063
AA2	−0.058
AB1	−0.139
AB2	−0.129
AB3	−0.055
AB4	−0.064

 This journal is © the Owner Societies 2022

Published on 05 April 2022. Downloaded by Ankara University on 10/29/2022 10:51:31 AM.

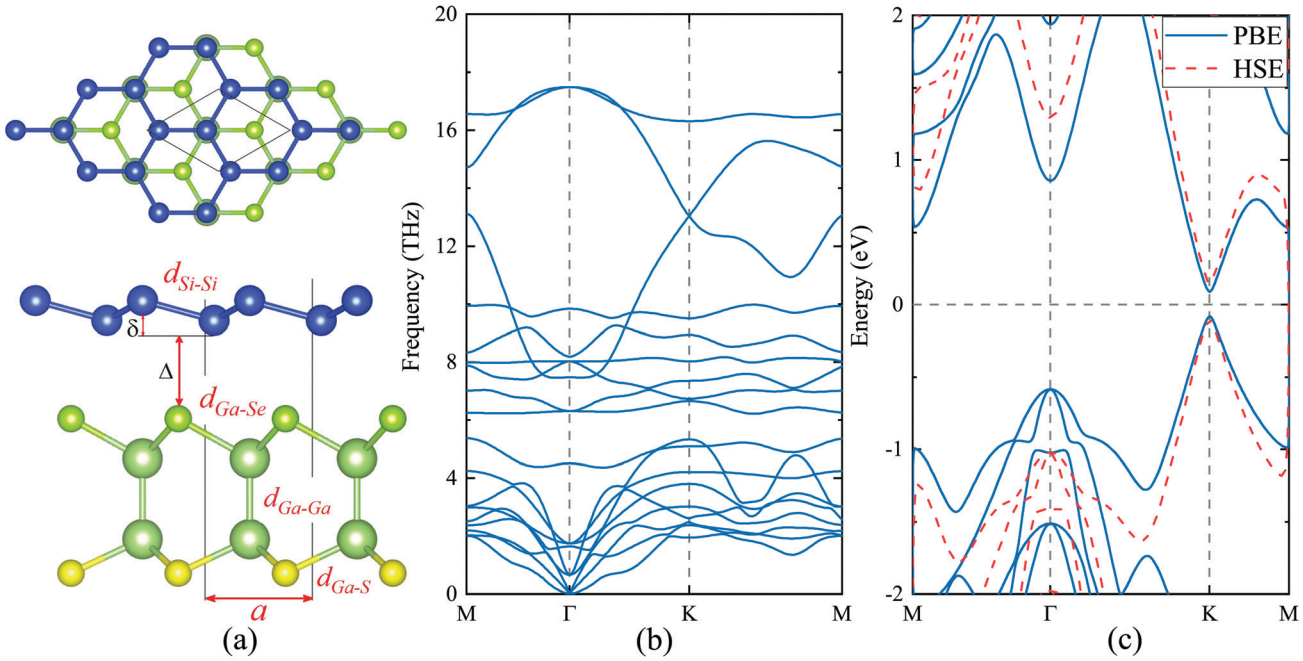


Fig. 2 (a) Top and side views, (b) phonon spectrum, and (c) electronic band structure of silicene/Ga_2SeS heterostructures.

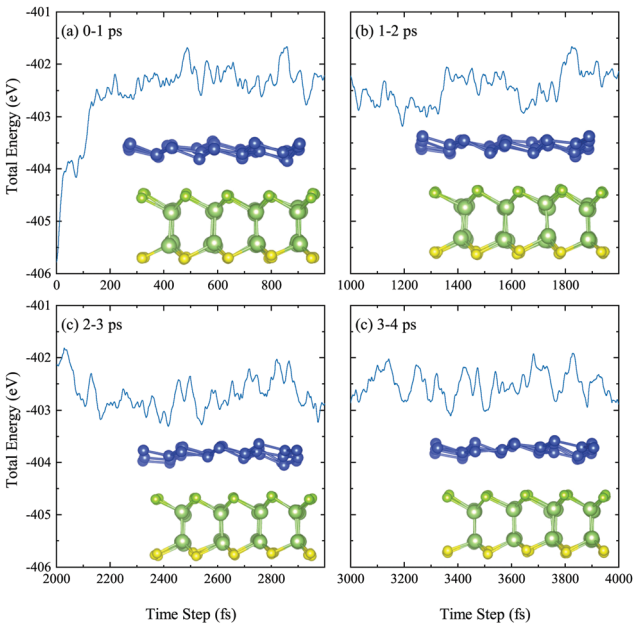


Fig. 3 The AIMD simulation of the total energy variation during the time interval of (a) 0–1, (b) 1–2, (c) 2–3, and (d) 3–4 ps at room temperature (300 K) (the insets in the graphs are snapshots of the corresponding time intervals).

structures is taken into account using the formula $\phi_w = E_{vac} - E_F$. Here E_{vac} and E_F indicate the vacuum and the Fermi energies, respectively. The work functions of silicene, Ga_2SeS, and the silicene/Ga_2SeS heterostructure are given in Fig. 6(b), and the results are consistent with previous studies.[25,65] It is known that the band alignments of vdW heterostructures are defined by the contributions of the layers to the VBM and CBM.[69] Thus, type-I band alignment occurs at the interface, as silicene contributes to both the CBM and VBM in the silicene/Ga_2SeS heterostructure. We also study the phenomenon which emerges in metal/semiconductor heterostructures called SBH. Based on the Schottky–Mott[39] formalism, there are two types of SBH called p-type and n-type. The p-type and n-type SBHs are determined by the formulas: $\phi_{B,p} = E_F - E_V^{SC}$ and $\phi_{B,n} = E_C^{SC} - E_F$, respectively, where E_F is the Fermi energy, E_C^{SC} is the conduction band offset (CBO) of the semiconductor, and E_V^{SC} is the valence band offset (VBO) of the semiconductor. We found the $\phi_{B,p}$ ($\phi_{B,n}$) SBHs for the silicene/Ga_2SeS heterostructure to be 0.923 eV (0.841 eV), indicating that the heterostructure is an n-type Schottky contact. The potential step (ΔV) of the interface is determined by the formula: $\Delta V = \varphi_{silicene/Ga2SeS} - \varphi_{silicene}$. The potential step at the interface is related to the charge transfer between the layers, *i.e.*, greater charge transfer means a higher potential step. The potential step (ΔV) across the interface of the silicene/Ga_2SeS heterostructure is 0.26 eV (in Fig. 6(b)), which is similar to that of GaSe/graphene.[43] Electron affinity (χ) and ionization potential (IP) influence the band alignment of heterostructures, which is crucial for device performance. Thus we have calculated both electron affinity and ionization potential of silicene/Ga_2SeS heterostructures, which are given in Fig. 6(b), by using the formulas $\chi_{Ga2SeS} = E_{vac} - E_C^{SC}$ and $IP_{Ga2SeS} = E_{vac} - E_V^{SC}$, respectively.[70]

The carrier mobility is a parameter that is essential for efficiency in electronic,[71–73] photovoltaic[74,75] and photocatalytic[76–78] applications. However, most semiconductors have low carrier mobilities,[79] which restrict their feasibility in nano-electronic applications. Hence, it is crucial to increase the carrier mobility for applications in next-generation technologies. Here, we have investigated the electron and hole mobilities of Ga_2SeS and the silicene/Ga_2SeS

Published on 05 April 2022. Downloaded by Ankara University on 10/29/2022 10:51:31 AM.

Table 2 Structural parameters of silicene, Ga_2SeS and the silicene/Ga_2SeS heterostructure (lattice constant (a), buckling height (δ, Å), interlayer distance (Δ), binding energy (E_b), bond lengths (d), electronic band gap (E), interlayer charge transfer (ΔQ), and total dipole moment (μ))

	a (Å)	δ (Å)	Δ (Å)	E_b (eV)	d_{Si-Si} (Å)	d_{Ga-Ga} (Å)	d_{Ga-S} (Å)	d_{Ga-Se} (Å)	E^{PBE} (eV)	E^{HSE} (eV)	ΔQ ($\lvert e\rvert$)	μ (eÅ)
Silicene	3.868	0.468	—	—	2.271	—	—	—	SM[a]	0.034	—	0
Ga_2SeS	3.731	—	—	—	—	2.438	2.372	2.452	2.392[b]	3.180[b]	—	−0.016
Silicene/Ga_2SeS	3.746	0.597	2.978	−0.139	2.244	2.442	2.396	2.476	0.165	0.215	0.024	−0.017

[a] Semi-metallic. [b] Indirect band gap.

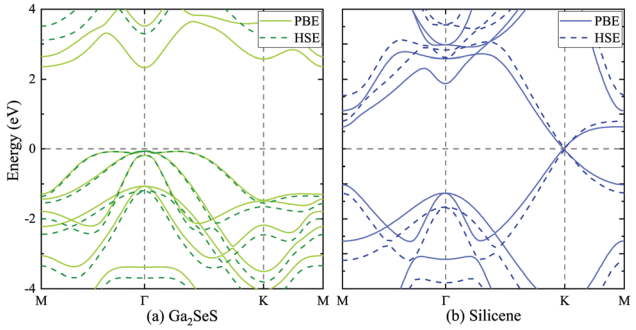


Fig. 4 The electronic band structures of pristine (a) Ga_2SeS and (b) silicene in both PBE and HSE06 methods.

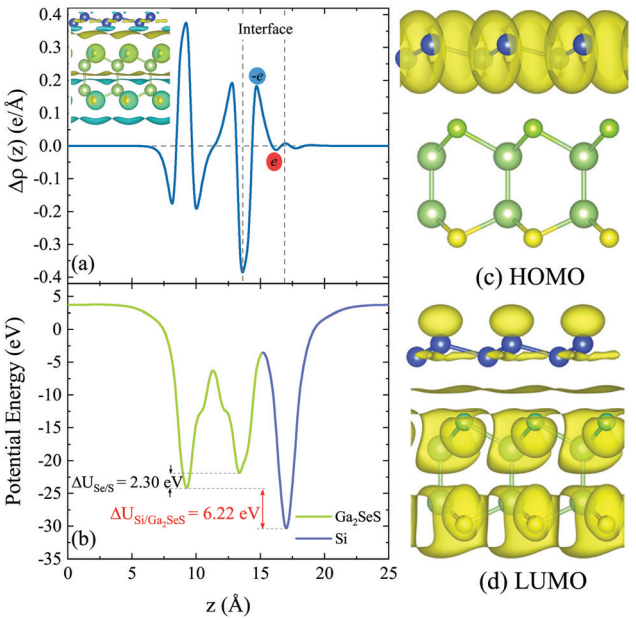


Fig. 5 (a) Plane-averaged charge density difference (the inset shows the isosurface with a charge density difference between silicene and Ga_2SeS layers of 0.002 eÅ^{-3}; the yellow and blue colors indicate electron accumulation and depletion, respectively), (b) plane-averaged electrostatic potential of the silicene/Ga_2SeS heterostructure, and (c) and (d) band-decomposed charge-density differences.

heterostructure *via* the DPT within the effective mass approximation. First, we consider an orthogonal unit cell for applying uniaxial strain in the range of −2% to 2% with an interval of 0.5% in the x (zigzag) and y (armchair) directions. The calculated band structures of orthogonal pristine Ga_2SeS and the silicene/Ga_2SeS heterostructure are presented in Fig. S1 (ESI†). We have calculated the effective electron (m_e^*) and hole (m_h^*) masses by using the equation presented in the Method section. It is known that the stronger dispersion of the VBM and CBM denotes small effective mass or *vice versa*. Also, there is a negative correlation between effective mass and carrier mobility, *i.e.*, a small (high) effective mass indicates a high (small) carrier mobility.[76,78] We listed the essential parameters required to find carrier mobility (effective mass (m^*) and deformation potential (E_1)), and in-plane stiffness ($C_{2D,x}$) in Table 3. For monolayer Ga_2SeS, as expected the hole effective mass is found to be larger than the electron effective mass due to the flat-like VBM (see Fig. S1 in the ESI†) in both directions. The in-plane stiffness values of x and y directions are found to be 74.836 and 74.840 N m^{-1}, respectively, as presented in Fig. S2 (ESI†). Besides, as also depicted in Fig. S3 (ESI†), the deformation potentials for electrons and holes are calculated as 8.908 (8.906) eV and 1.629 (1.976) eV for x and y directions, respectively. Consequently, the electron (hole) mobility is ∼500 (∼200) cm^2 V^{-1} s^{-1}, which is comparable to previous results of monolayer GaSe.[80–82] Besides, it is well known that silicene has superior electron and hole mobility, around 2×10^5 cm^2 V^{-1} s^{-1} [83] at room temperature. For the silicene/Ga_2SeS heterostructure, the electron and hole effective masses are much lower than those in the Ga_2SeS one. This is because the silicene layer contributes to the VBM and CBM, making the dispersion stronger. The deformation potential of electrons (holes) is decreased (increased) for the silicene/Ga_2SeS heterostructure. In comparison to the pristine Ga_2SeS case, the electronic band structure of the silicene/Ga_2SeS heterostructure is less responsive to strain. In addition, the in-plane stiffness of the silicene/Ga_2SeS heterostructure increased in both directions. With decreasing effective electron and hole masses, deformation potentials, and increasing in-plane stiffness, the carrier mobility increased dramatically. Consequently, it can be concluded that the carrier mobility of Ga_2SeS may be improved by stacking with silicene, thus widening the application range.

B The electronic properties under external electric field effects

It is crucial to tune the electronic properties of heterostructures to propose multi-purpose high-performance devices. We, therefore, examine the variation of the electronic properties and SBHs of the silicene/Ga_2SeS heterostructure in the presence of an external electric field. The layer decomposed electronic band spectrum of the silicene/Ga_2SeS heterostructure under an external electric field is presented in Fig. 7(a)–(g). By increasing the magnitude of the positive (negative) electric field, the band

 This journal is © the Owner Societies 2022

Published on 05 April 2022. Downloaded by Ankara University on 10/29/2022 10:51:31 AM.

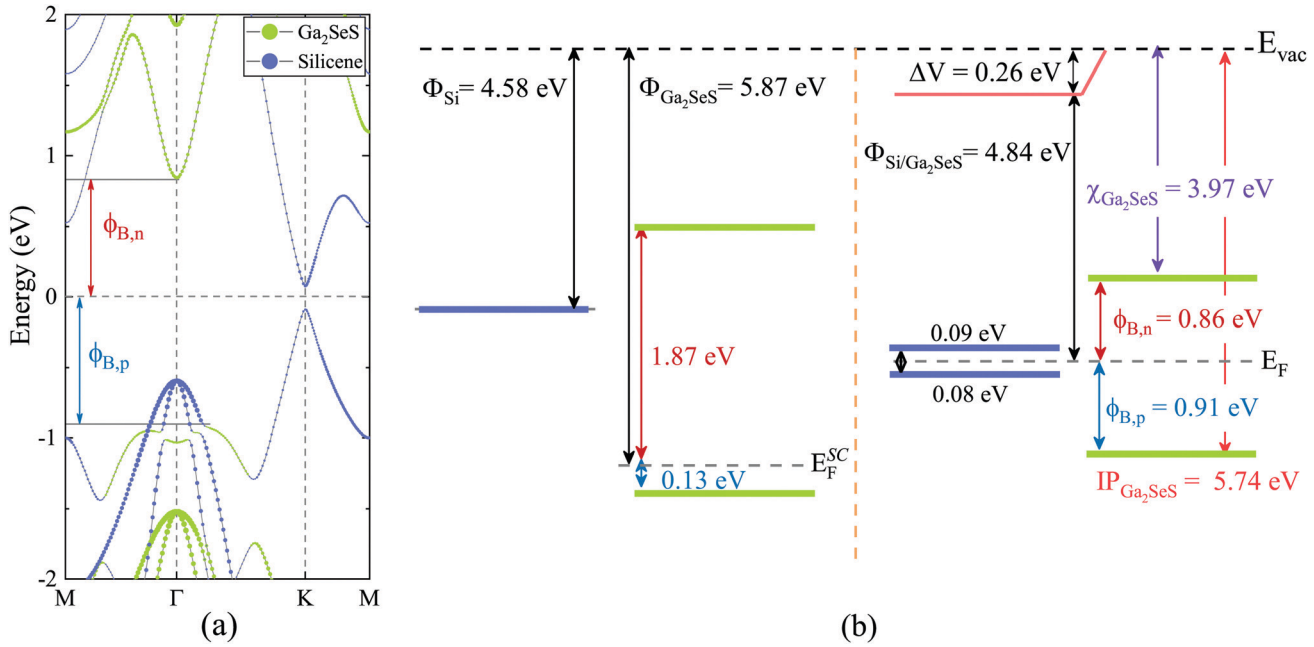


Fig. 6 (a) The layer decomposed projected electronic band structure and (b) the illustration of band alignment of the silicene/Ga_2SeS heterostructure.

Table 3 Calculated effective mass m^* (m_0), deformation potential E_1 (eV), in-plane stiffness $C_{2D,x}$ (N m^{-1}) and carrier mobility ($\bar{\mu}$) (10^3 cm^2 V^{-1} s^{-1}) of electrons and holes in the zigzag (x) and armchair (y) directions at room temperature (300 K) for monolayer Ga_2SeS and the silicene/Ga_2SeS heterostructure

	m_x^*	m_y^*	$E_{1,x}$	$E_{1,y}$	$C_{2D,x}$	$C_{2D,y}$	$\bar{\mu}_x$	$\bar{\mu}_y$
Electron								
Ga_2SeS	0.210	0.193	8.908	8.906	74.836	74.840	0.479	0.522
Silicene/Ga_2SeS	0.148	0.169	3.806	3.784	142.108	141.942	14.664	7.943
Hole								
Ga_2SeS	1.767	2.231	1.629	1.976	74.836	74.840	0.212	0.115
Silicene/Ga_2SeS	0.159	0.182	2.951	2.964	142.108	141.942	12.684	11.172

gap decreases (increases) with a retained direct band gap. However, at -0.9 V Å^{-1}, the heterostructure becomes metallic, and the free electron-like parabolic band occurs at Γ, which crosses the Fermi level. In the plane-wave approximation (PW), the plane-averaged potential diverges due to the periodic boundary conditions in the excess negative charge injection. Therefore, the excess electrons created by the negative charge injection (external negative electric field) are located in free electron-like bands.[84] In the atomic orbital (AO) approximation, local atomic orbitals exist only in atomic regions and hence do not contain excessive electrons. Hence, the free-electron-like parabolic bands do not form. Therefore, we have considered electronic band structures in the presence of the electric field in the AO-based OpenMX 3.9 package.[85] The comparison of electronic band structures calculated with PW- and AO-based programs is presented in Fig. S4 (see the ESI†). The electronic band structures in the presence of the electric field are nearly the same for all-electric field magnitudes, except for -0.9 V Å^{-1}, which is fixed by AO-based calculations.

As presented in Fig. 7(a)–(g), when the applied electric field varies from -0.9 to 0.9 V Å^{-1}, the CBO and VBO of silicene slightly decrease, while the CBO and VBO of Ga_2SeS gradually increase. The direction and magnitude of the electric field affect the variation of the dipole moment. We, therefore, investigated the evolution of the dipole moment of the silicene/Ga_2SeS heterostructure. The external positive electric field in the silicene/Ga_2SeS heterostructure is anti-parallel to the intrinsic electric field. Herein, the positive electric field weakens the total dipole moment, while the negative electric field strengthens it without changing its direction. Further, we present in Fig. 7(i) interlayer charge transfer in the presence of an external electric field by means of Bader charge analysis. The charge transfer from silicene to Ga_2SeS decreases as the electric field magnitude changes from -0.9 V Å^{-1} to 0.6 V Å^{-1}, and when it reaches 0.9 V Å^{-1}, the charge transfer direction changes. Furthermore, we investigate the evolution of SBH under an external electric field. As we mentioned earlier, the CBO and VBO of Ga_2SeS are essential to determine SBHs. Hence, as the CBO and VBO of Ga_2SeS vary under the external electric field, the Schottky barrier type of Ga_2SeS is altered. As depicted in Fig. 7(j), the SBH changes under the applied external electric field, *i.e.*, with the applied electric field in the

Published on 05 April 2022. Downloaded by Ankara University on 10/29/2022 10:51:31 AM.

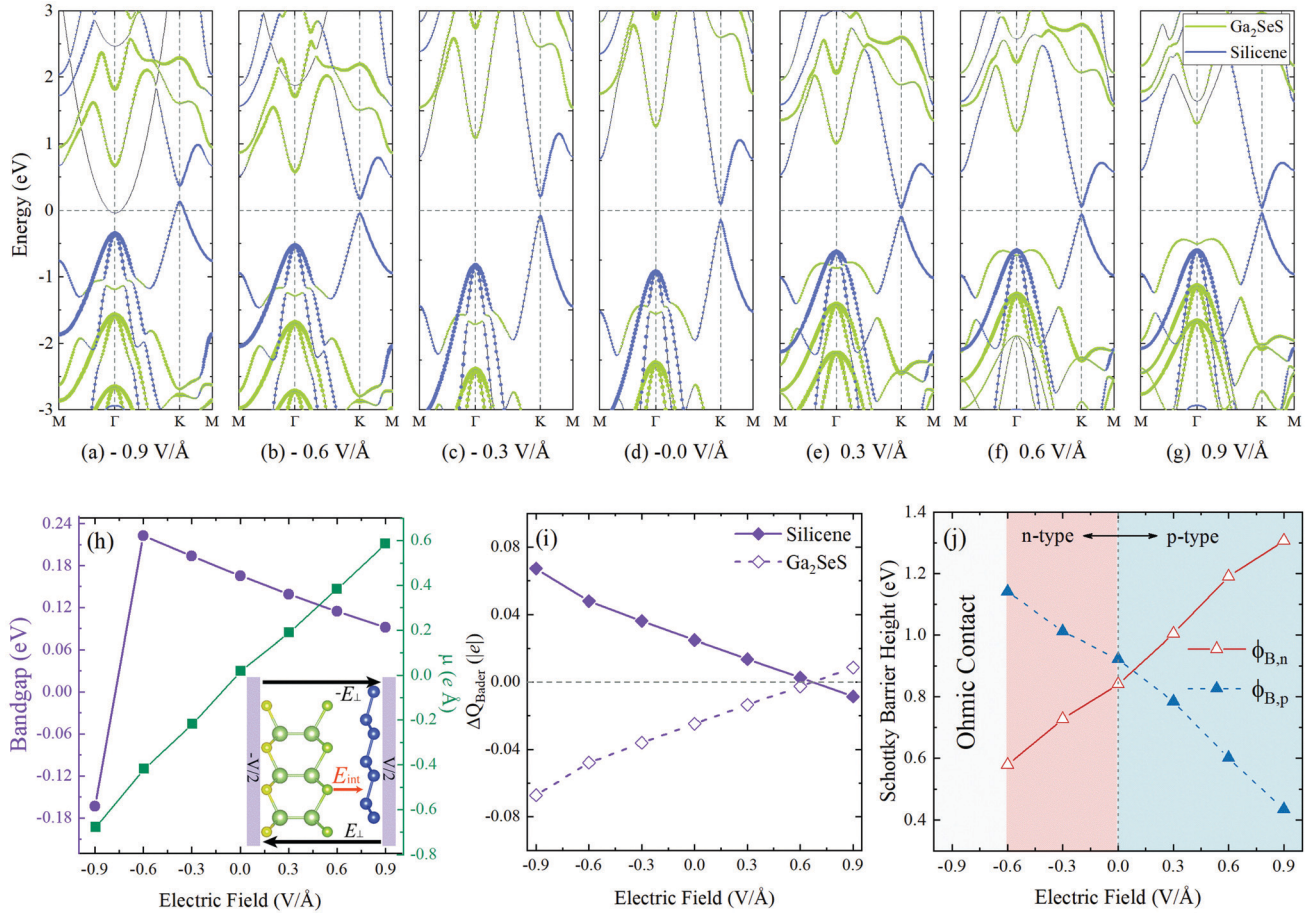


Fig. 7 (a)–(g) The electronic band spectrum, the variation of (h) band gaps and dipole moments, (i) the interlayer charge transfer, and (j) the Schottky barrier heights in the presence of a perpendicular electric field (the inset in (h) shows the schematic illustration of the perpendicular electric field).

positive direction, the SBH of the silicene/Ga_2SeS heterostructure changes instantly from n-type to p-type. Except for -0.9 V Å^{-1}, where the silicene/Ga_2SeS heterostructure alters to an ohmic contact, the n-type SBH is maintained under the applied negative electric field. This behavior of the SBH of silicene/Ga_2SeS is different from that of the graphene/Ga_2 SSe heterostructure.[86] In the graphene case, the SBH changes to p-type (n-type) with an applied negative (positive) electric field contrary to the silicene case.

C The electronic properties under biaxial strain

In the quest for modulating the electronic properties of 2D heterostructures, biaxial strain is one of these. Hence, we have examined the electronic properties of the silicene/Ga_2SeS heterostructure under biaxial strain. We apply biaxial strains from -4% to 8% at 2% intervals, by using the strain formula: $\varepsilon = (a' - a)/a'$, where a' and a are the strained and unstrained lattice constants, respectively. We have given the evolution of structural parameters in the presence of biaxial strain in Table 4. With the increasing magnitude of tensile (compressive) strain, the buckling height of silicene decreases (increases), whereas the bond lengths and angles increase (decrease). In the meantime, the bond lengths and angles of Ga–S and Ga–Se increase between 4% and 8% strain magnitudes. Alterations in structural parameters straightly influence the electronic band structures as can also be seen in Fig. 8(a)–(g) which show the layer decomposed electronic band structures of the silicene/Ga_2SeS heterostructure. Between -2% and 6% strain magnitudes, the CBM and VBM shift towards the Fermi level, resulting in the evolution of band gaps shown in Fig. 8(h). At the maximum compressive (-4%) and tensile (8%) strain magnitudes, the electronic band structure of silicene/Ga_2SeS becomes metallic. We also study the dipole moment variations in the presence of biaxial strain. The evolution of total dipole moments is

Table 4 The evolution of structural parameters in the presence of biaxial strain (strained lattice constant (a'), buckling height (δ), interlayer distance (Δ),bond lengths (d), and bond angles ($\angle$))

ε (%)	a' (Å)	δ (Å)	Δ (Å)	d_{Si-Si} (Å)	$\angle$ Si–Si (°)	d_{Ga-S} (Å)	$\angle$ Ga–S (°)	d_{Ga-Se} (Å)	$\angle$ Ga–Se (°)
−4	3.596	0.762	2.916	2.212	108.781	2.352	99.720	2.439	94.993
−2	3.671	0.673	2.958	2.223	111.255	2.373	101.313	2.457	96.687
0	3.746	0.596	2.978	2.244	113.190	2.396	102.857	2.476	98.297
2	3.821	0.523	2.995	2.267	114.853	2.418	104.363	2.497	99.826
4	3.896	0.455	3.001	2.295	116.182	2.441	105.864	2.519	101.295
6	3.971	0.400	2.995	2.327	117.107	2.464	107.363	2.542	102.688
8	4.046	0.369	2.971	2.365	117.610	2.487	108.847	2.567	104.017

This journal is © the Owner Societies 2022

Published on 05 April 2022. Downloaded by Ankara University on 10/29/2022 10:51:31 AM.

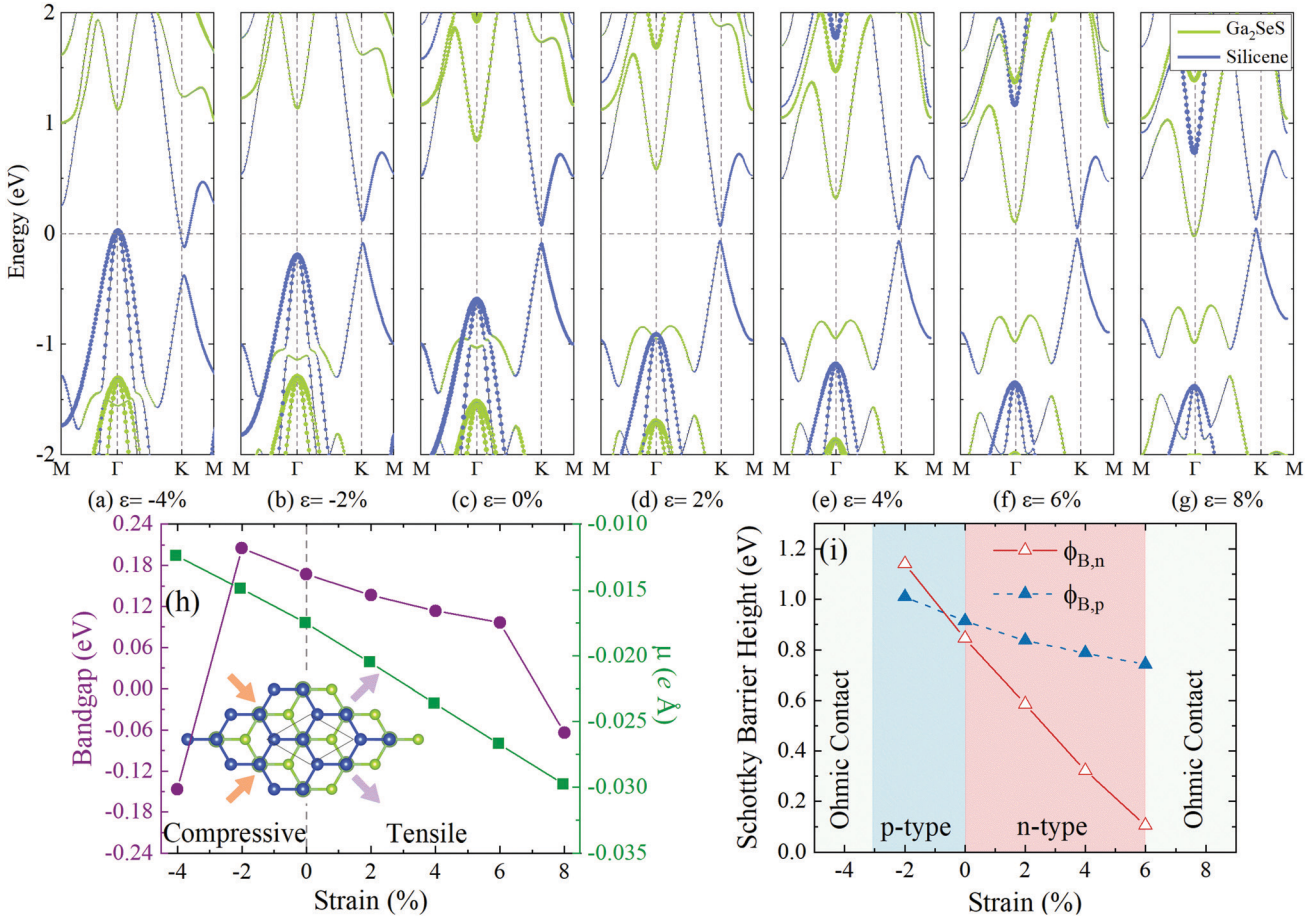


Fig. 8 (a)–(g) The layer decomposed electronic band structures, the evolution of (i) band gaps and total dipole moments, and (i) the Schottky barrier heights of the silicene/Ga_2SeS heterostructure under biaxial strain.

demonstrated in Fig. 8(h). The total dipole moment decreases with increasing tensile strain magnitude while being enhanced with increasing compressive strain magnitude. The variation of interlayer distances is associated with the dipole moments of the structure. Therefore, as shown in Fig. 8(h), the total dipole moment changes with the evolution of interlayer distances under the biaxial strain, as given in Table 4. We further investigate whether the SBH of silicene/Ga_2SeS is tunable in the presence of the biaxial strain. When compressive strain is applied to the silicene/Ga_2SeS heterostructure, the CBO and VBO of Ga_2SeS shift upward and downward toward the Fermi level, respectively. As a result of changes in band offsets, the SBH switches from n-type to p-type, then to an ohmic contact, as can be seen in Fig. 8(i). In contrast, when tensile strain is applied, the CBO and VBO of Ga_2SeS shift towards the Fermi level and switch to an ohmic contact when the SBH strain magnitude reaches 8%.

IV Conclusion

In summary, we examine the effect of the intrinsic electric field of Ga_2SeS on the Schottky barrier formed in the silicene/Ga_2SeS heterostructure. In the pristine case, although the n-type Schottky barrier is formed, which is similar to the silicene/GaSe heterostructure, the SBH is altered. This can be attributed to the intrinsic electric field in Ga_2SeS. Further, we investigate whether the Schottky barrier height of the silicene/Ga_2SeS heterostructure can be tuned with electric field and strain. Accordingly, we analyze the variation of the electronic band gap, interlayer charge transfer, total dipole moment, and p-type/n-type Schottky barrier height of the silicene/Ga_2SeS heterostructure under external effects. With an applied positive electric field to the silicene/Ga_2SeS heterostructure, the Schottky barrier instantaneously changes from n-type to p-type, while, with a negative electric field, the Schottky barrier remains n-type until -0.9 V Å^{-1} which is the value of the transition from the Schottky contact to an ohmic contact. Moreover, a transition from n-type to p-type is observed when compressive strain is applied to the silicene/Ga_2SeS heterostructure. Eventually, the effect of the external electric field and biaxial strain on the silicene/Ga_2SeS heterostructure has a critical impact on the tuning of Schottky barrier height and hence the device performance.

Conflicts of interest

There are no conflicts to declare.

Published on 05 April 2022. Downloaded by Ankara University on 10/29/2022 10:51:31 AM.

Acknowledgements

This work was supported by the Ankara University BAP research project under Project No. 21B0443001. The calculations were performed at TUBITAK ULAKBIM, High Performance and Grid Computing Center (TR-Grid e-Infrastructure).

References

1 X. H. Li, B. J. Wang, H. Li, X. F. Yang, R. Q. Zhao and X. T. Jia, *et al.*, Two-dimensional layered Janus-In_2SeTe/C_2N van der Waals heterostructures for photocatalysis and photovoltaics: first-principles calculations, *New J. Chem.*, 2020, **44**, 16092–16100, DOI: **10.1039/D0NJ03296D**.

2 I. Bouziani, M. Kibbou, Z. Haman, N. Khossossi, I. Essaoud, A. Ainane and R. Ahuja, Two-dimensional Janus Sn_2SSe and $SnGeS_2$ semiconductors as strong absorber candidates for photovoltaic solar cells: First principles computations, *Phys. E*, 2021, **134**, 114900. Available from: **https://www.sciencedirect.com/science/article/pii/S1386947721002757**.

3 H. Zhao, Y. Gu, N. Lu, Y. Liu, Y. Ding and B. Ye, *et al.*, Janus In_2SeTe for photovoltaic device applications from first-principles study, *Chem. Phys.*, 2022, **553**, 111384. Available from: **https://www.sciencedirect.com/science/article/pii/S0301010421002950**.

4 J. Wang, H. Guo, J. Xue, D. Chen, G. Yang and B. Liu, *et al.*, Janus Ga_2SeTe: A Promising Candidate for Highly Efficient Solar Cells, *Solar RRL*, 2019, **3**(12), 1900321. Available from: **https://onlinelibrary.wiley.com/doi/abs/10.1002/solr.201900321**.

5 Y. Ji, M. Yang, H. Lin, T. Hou, L. Wang and Y. Li, *et al.*, Janus Structures of Transition Metal Dichalcogenides as the Heterojunction Photocatalysts for Water Splitting, *J. Phys. Chem. C*, 2018, **122**(5), 3123–3129, DOI: **10.1021/acs.jpcc.7b11584**.

6 R. Peng, Y. Ma, B. Huang and Y. Dai, Two-dimensional Janus PtSSe for photocatalytic water splitting under the visible or infrared light, *J. Mater. Chem. A*, 2019, **7**, 603–610, DOI: **10.1039/C8TA09177C**.

7 R. da Silva, R. Barbosa, R. R. Mançano, N. Durães, R. B. Pontes and R. H. Miwa, *et al.*, Metal Chalcogenides Janus Monolayers for Efficient Hydrogen Generation by Photocatalytic Water Splitting, *ACS Appl. Nano Mater.*, 2019, **2**(2), 890–897, DOI: **10.1021/acsanm.8b02135**.

8 R. Chaurasiya and A. Dixit, Defect engineered MoSSe Janus monolayer as a promising two dimensional material for NO2 and NO gas sensing, *Appl. Surf. Sci.*, 2019, **490**, 204–219. Available from: **https://www.sciencedirect.com/science/article/pii/S016943321931743X**.

9 D. Wang, T. Lan, J. Pan, Z. Liu, A. Yang and M. Yang, *et al.*, Janus MoSSe monolayer: a highly strain-sensitive gas sensing material to detect SF6 decompositions, *Sens. Actuators, A*, 2020, **311**, 112049. Available from: **https://www.sciencedirect.com/science/article/pii/S0924424720303083**.

10 K. Pang, Y. Wei, W. Li, X. Zhou, Y. Jiang and J. Yang, *et al.*, Highly sensitive gas sensing material for polar gas molecule based on Janus group-III chalcogenide monolayers: a first-principles investigation, *Sci. China Technological Sci.*, 2020, **63**(8), 1566–1576. Available from: **https://link.springer.com/article/10.1007/s11431-020-1616-9**.

11 D. B. Trivedi, G. Turgut, Y. Qin, M. Y. Sayyad, D. Hajra and M. Howell, *et al.*, Room-Temperature Synthesis of 2D Janus Crystals and their Heterostructures, *Adv. Mater.*, 2020, **32**(50), 2006320. Available from: **https://onlinelibrary.wiley.com/doi/abs/10.1002/adma.202006320**.

12 A. Y. Lu, H. Zhu, J. Xiao, C. P. Chuu, Y. Han and M. H. Chiu, *et al.*, Janus monolayers of transition metal dichalcogenides, *Nat. Nanotechnol.*, 2017, **12**(8), 744–749. Available from: **https://www.nature.com/articles/nnano.2017.100**.

13 J. Zhang, S. Jia, I. Kholmanov, L. Dong, D. Er and W. Chen, *et al.*, Janus Monolayer Transition-Metal Dichalcogenides, *ACS Nano*, 2017, **11**(8), 8192–8198, DOI: **10.1021/acsnano.7b03186**, PMID: 28771310.

14 Y. C. Lin, C. Liu, Y. Yu, E. Zarkadoula, M. Yoon and A. A. Puretzky, *et al.*, Low Energy Implantation into Transition-Metal Dichalcogenide Monolayers to Form Janus Structures, *ACS Nano*, 2020, **14**(4), 3896–3906, DOI: **10.1021/acsnano.9b10196**.

15 Y. Ma, Y. Dai, M. Guo, L. Yu and B. Huang, Tunable electronic and dielectric behavior of GaS and GaSe monolayers, *Phys. Chem. Chem. Phys.*, 2013, **15**, 7098–7105, DOI: **10.1039/C3CP50233C**.

16 G. W. Mudd, S. A. Svatek, T. Ren, A. Patanè, O. Makarovsky and L. Eaves, *et al.*, Tuning the Bandgap of Exfoliated InSe Nanosheets by Quantum Confinement, *Adv. Mater.*, 2013, **25**(40), 5714–5718. Available from: **https://onlinelibrary.wiley.com/doi/abs/10.1002/adma.201302616**.

17 J. Lauth, F. E. S. Gorris, M. Samadi Khoshkhoo, T. Chassé, W. Friedrich and V. Lebedeva, *et al.*, Solution-Processed Two-Dimensional Ultrathin InSe Nanosheets, *Chem. Mater.*, 2016, **28**(6), 1728–1736, DOI: **10.1021/acs.chemmater.5b04646**.

18 D. J. Late, B. Liu, H. S. S. R. Matte, C. N. R. Rao and V. P. Dravid, Rapid Characterization of Ultrathin Layers of Chalcogenides on SiO_2/Si Substrates, *Adv. Funct. Mater.*, 2012, **22**(9), 1894–1905. Available from: **https://onlinelibrary.wiley.com/doi/abs/10.1002/adfm.201102913**.

19 S. Demirci, N. Avazl, E. Durgun and S. Cahangirov, Structural and electronic properties of monolayer group III monochalcogenides, *Phys. Rev. B*, 2017, **95**, 115409, DOI: **10.1103/PhysRevB.95.115409**.

20 M. Bernardi, C. Ataca, M. Palummo and J. C. Grossman, Optical and Electronic Properties of Two-Dimensional Layered Materials, *Nanophotonics*, 2017, **6**(2), 479–493, DOI: **10.1515/nanoph-2015-0030**.

21 P. Hu, L. Wang, M. Yoon, J. Zhang, W. Feng and X. Wang, *et al.*, Highly Responsive Ultrathin GaS Nanosheet Photodetectors on Rigid and Flexible Substrates, *Nano Lett.*, 2013, **13**(4), 1649–1654, DOI: **10.1021/nl400107k**.

22 L. Hu and D. Wei, Janus Group-III Chalcogenide Monolayers and Derivative Type-II Heterojunctions as Water-Splitting Photocatalysts with Strong Visible-Light Absorbance, *J. Phys. Chem. C*, 2018, **122**(49), 27795–27802, DOI: **10.1021/acs.jpcc.8b06575**.

 This journal is © the Owner Societies 2022

Published on 05 April 2022. Downloaded by Ankara University on 10/29/2022 10:51:31 AM.

23 A. Kandemir and H. Sahin, Janus single layers of In_2SSe: a first-principles study, *Phys. Rev. B*, 2018, **97**, 155410. Available from: **https://link.aps.org/doi/10.1103/PhysRevB.97.155410**.

24 R. Li, Y. Cheng and W. Huang, Recent Progress of Janus 2D Transition Metal Chalcogenides: From Theory to Experiments, *Small.*, 2018, **14**(45), 1802091. Available from: **ttps://onlinelibrary.wiley.com/doi/abs/10.1002/smll.201802091**.

25 H. D. Bui, H. R. Jappor and N. N. Hieu, Tunable optical and electronic properties of Janus monolayers Ga_2SSe, Ga_2STe, and Ga_2SeTe as promising candidates for ultraviolet photodetectors applications, *Superlattices Microstruct.*, 2019, **125**, 1–7. Available from: **https://www.sciencedirect.com/science/article/pii/S074960361831961X**.

26 B. Lalmi, H. Oughaddou, H. Enriquez, A. Kara, S. Vizzini and B. Ealet, *et al.*, Epitaxial growth of a silicene sheet, *Appl. Phys. Lett.*, 2010, **97**(22), 223109, DOI: **10.1063/1.3524215**.

27 H. Okamoto, Y. Sugiyama and H. Nakano, Synthesis and Modification of Silicon Nanosheets and Other Silicon Nanomaterials, *Chem. – Eur. J.*, 2011, **17**(36), 9864–9887. Available from: **https://chemistry-europe.onlinelibrary.wiley.com/doi/abs/10.1002/chem.201100641**.

28 P. Vogt, P. De Padova, C. Quaresima, J. Avila, E. Frantzeskakis and M. C. Asensio, *et al.*, Silicene: Compelling Experimental Evidence for Graphenelike Two-Dimensional Silicon, *Phys. Rev. Lett.*, 2012, **108**, 155501. Available from: **https://link.aps.org/doi/10.1103/PhysRevLett.108.155501**.

29 B. Feng, Z. Ding, S. Meng, Y. Yao, X. He and P. Cheng, *et al.*, Evidence of Silicene in Honeycomb Structures of Silicon on Ag(111), *Nano Lett.*, 2012, **12**(7), 3507–3511, DOI: **10.1021/nl301047g**.

30 R. Friedlein and Y. Yamada-Takamura, Electronic properties of epitaxial silicene on diboride thin films, *J. Phys.: Condens. Matter*, 2015, **27**(20), 203201, DOI: **10.1088/0953-8984/27/20/203201**.

31 L. Chen, C. C. Liu, B. Feng, X. He, P. Cheng and Z. Ding, *et al.*, Evidence for Dirac Fermions in a Honeycomb Lattice Based on Silicon, *Phys. Rev. Lett.*, 2012, **109**, 056804. Available from: **https://link.aps.org/doi/10.1103/PhysRevLett.109.056804**.

32 E. Zaminpayma and P. Nayebi, Band gap engineering in silicene: a theoretical study of density functional tight-binding theory, *Phys. E*, 2016, **84**, 555–563. Available from: **https://www.sciencedirect.com/science/article/pii/S1386947716301667**.

33 A. Molle, C. Grazianetti, L. Tao, D. Taneja, M. H. Alam and D. Akinwande, Silicene, silicene derivatives, and their device applications, *Chem. Soc. Rev.*, 2018, **47**, 6370–6387, DOI: **10.1039/C8CS00338F**.

34 H. Chen, J. Zhao, J. Huang and Y. Liang, Computational understanding of the structural and electronic properties of the GeS-graphene contact, *Phys. Chem. Chem. Phys.*, 2019, **21**, 7447–7453, DOI: **10.1039/C9CP00374F**.

35 W. Chen, F. Wang, S. Qin, J. Fang, C. Wang and G. Wang, *et al.*, Observation of complete space-charge-limited transport in metal-oxide-graphene heterostructure, *Appl. Phys. Lett.*, 2015, **106**(2), 023122, DOI: **10.1063/1.4906202**.

36 O. Lopez-Sanchez, D. Lembke, M. Kayci, A. Radenovic and A. Kis, Ultrasensitive photodetectors based on monolayer MoS_2, *Nat. Nanotechnol.*, 2013, **8**(7), 497–501, DOI: **10.1038/nnano.2013.100**.

37 X. Li, H. Zhu, K. Wang, A. Cao, J. Wei and C. Li, *et al.*, Graphene-On-Silicon Schottky Junction Solar Cells, *Adv. Mater.*, 2010, **22**(25), 2743–2748. Available from: **https://onlinelibrary.wiley.com/doi/abs/10.1002/adma.200904383**.

38 H. Y. Kim, K. Lee, N. McEvoy, C. Yim and G. S. Duesberg, Chemically Modulated Graphene Diodes, *Nano Lett.*, 2013, **13**(5), 2182–2188, DOI: **10.1021/nl400674k**.

39 R. T. Tung, The physics and chemistry of the Schottky barrier height, *Appl. Phys. Rev.*, 2014, **1**(1), 011304.

40 V. Van Quang, N. Van Dung, N. Sy Trong, N. Duc Hoa, N. Van Duy and N. Van Hieu, Outstanding gas-sensing performance of graphene/SnO_2 nanowire Schottky junctions, *Appl. Phys. Lett.*, 2014, **105**(1), 013107, DOI: **10.1063/1.4887486**.

41 J. Kwon, J. Y. Lee, Y. J. Yu, C. H. Lee, X. Cui and J. Hone, *et al.*, Thickness-dependent Schottky barrier height of MoS_2 field-effect transistors, *Nanoscale*, 2017, **9**, 6151–6157, DOI: **10.1039/C7NR01501A**.

42 C. He, M. Cheng, T. Li and W. Zhang, Tunable Ohmic, p-Type Quasi-Ohmic, and n-Type Schottky Contacts of Monolayer SnSe with Metals, *ACS Appl. Nano Mater.*, 2019, **2**(5), 2767–2775, DOI: **10.1021/acsanm.9b00276**.

43 C. Si, Z. Lin, J. Zhou and Z. Sun, Controllable Schottky barrier in GaSe/graphene heterostructure: the role of interface dipole, *2D Mater.*, 2016, **4**(1), 015027, DOI: **10.1088/2053-1583/4/1/015027**.

44 F. Zhang, W. Li, Y. Ma, Y. Tang and X. Dai, Tuning the Schottky contacts at the graphene/WS_2 interface by electric field, *RSC Adv.*, 2017, **7**, 29350–29356, DOI: **10.1039/C7RA00589J**.

45 R. Caglayan, Y. Mogulkoc, A. Mogulkoc and B. Alkan, First principles study on optoelectronic properties of energetically stable Si/InS van der Waals heterobilayers, *J. Mater. Sci.*, 2020, **55**(31), 15199–15212, DOI: **10.1007/s10853-020-05094-4**.

46 H. Li, Z. Zhou and H. Wang, Tunable Schottky barrier in InTe/graphene van der Waals heterostructure, *Nanotechnology*, 2020, **31**(33), 335201, DOI: **10.1088/1361-6528/ab8e77**.

47 W. Xiong, C. Xia, X. Zhao, T. Wang and Y. Jia, Effects of strain and electric field on electronic structures and Schottky barrier in graphene and SnS hybrid heterostructures, *Carbon*, 2016, **109**, 737–746. Available from: **https://www.sciencedirect.com/science/article/pii/S0008622316307370**.

48 P. T. T. Le, N. N. Hieu, L. M. Bui, H. V. Phuc, B. D. Hoi and B. Amin, *et al.*, Structural and electronic properties of a van der Waals heterostructure based on silicene and gallium selenide: effect of strain and electric field, *Phys. Chem. Chem. Phys.*, 2018, **20**, 27856–27864, DOI: **10.1039/C8CP05588B**.

49 P. E. Blöchl, Projector augmented-wave method, *Phys. Rev. B: Condens. Matter Mater. Phys.*, 1994, **50**, 17953–17979. Available from: **https://link.aps.org/doi/10.1103/PhysRevB.50.17953**.

Published on 05 April 2022. Downloaded by Ankara University on 10/29/2022 10:51:31 AM.

50 G. Kresse and J. Hafner, Ab initio molecular dynamics for liquid metals, *Phys. Rev. B: Condens. Matter Mater. Phys.*, 1993, **47**, 558–561. Available from: **https://link.aps.org/doi/10.1103/PhysRevB.47.558**.

51 G. Kresse and J. Hafner, Ab initio molecular-dynamics simulation of the liquid-metal-amorphous-semiconductor transition in germanium, *Phys. Rev. B: Condens. Matter Mater. Phys.*, 1994, **49**, 14251–14269. Available from: **https://link.aps.org/doi/10.1103/PhysRevB.49.14251**.

52 G. Kresse and J. Furthmüller, Efficiency of ab initio total energy calculations for metals and semiconductors using a plane-wave basis set, *Comput. Mater. Sci.*, 1996, **6**(1), 15–50. Available from: **https://www.sciencedirect.com/science/article/pii/0927025696000080**.

53 G. Kresse and J. Furthmüller, Efficient iterative schemes for ab initio total-energy calculations using a plane-wave basis set, *Phys. Rev. B: Condens. Matter Mater. Phys.*, 1996, **54**, 11169–11186. Available from: **https://link.aps.org/doi/10.1103/PhysRevB.54.11169**.

54 J. P. Perdew, K. Burke and M. Ernzerhof, Generalized Gradient Approximation Made Simple, *Phys. Rev. Lett.*, 1996, **77**, 3865–3868. Available from: **https://link.aps.org/doi/10.1103/PhysRevLett.77.3865**.

55 J. Heyd, G. E. Scuseria and M. Ernzerhof, Hybrid functionals based on a screened Coulomb potential, *J. Chem. Phys.*, 2003, **118**(18), 8207–8215, DOI: **10.1063/1.1564060**.

56 A. V. Krukau, O. A. Vydrov, A. F. Izmaylov and G. E. Scuseria, Influence of the exchange screening parameter on the performance of screened hybrid functionals, *J. Chem. Phys.*, 2006, **125**(22), 224106, DOI: **10.1063/1.2404663**.

57 H. J. Monkhorst and J. D. Pack, Special points for Brillouin-zone integrations, *Phys. Rev. B: Condens. Matter Mater. Phys.*, 1976, **13**, 5188–5192. Available from: **https://link.aps.org/doi/10.1103/PhysRevB.13.5188**.

58 S. Grimme, Semiempirical GGA-type density functional constructed with a long-range dispersion correction, *J. Comput. Chem.*, 2006, **27**(15), 1787–1799. Available from: **https://onlinelibrary.wiley.com/doi/abs/10.1002/jcc.20495**.

59 W. Tang, E. Sanville and G. Henkelman, A grid-based Bader analysis algorithm without lattice bias, *J. Phys.: Condens. Matter*, 2009, **21**(8), 084204, DOI: **10.1088/0953-8984/21/8/084204**.

60 E. Sanville, S. D. Kenny, R. Smith and G. Henkelman, Improved grid-based algorithm for Bader charge allocation, *J. Comput. Chem.*, 2007, **28**(5), 899–908. Available from: **https://onlinelibrary.wiley.com/doi/abs/10.1002/jcc.20575**.

61 G. Henkelman, A. Arnaldsson and H. Jónsson, A fast and robust algorithm for Bader decomposition of charge density, *Comput. Mater. Sci.*, 2006, **36**(3), 354–360. Available from: **https://www.sciencedirect.com/science/article/pii/S0927025605001849**.

62 A. Togo and I. Tanaka, First principles phonon calculations in materials science, *Scr. Mater.*, 2015, **108**, 1–5. Available from: **https://www.sciencedirect.com/science/article/pii/S1359646215003127**.

63 J. Bardeen and W. Shockley, Deformation Potentials and Mobilities in Non-Polar Crystals, *Phys. Rev.*, 1950, **80**, 72–80. Available from: **https://link.aps.org/doi/10.1103/PhysRev.80.72**.

64 Y. Ding and Y. Wang, Electronic structures of silicene/GaS heterosheets, *Appl. Phys. Lett.*, 2013, **103**(4), 043114.

65 H. Liu, J. Gao and J. Zhao, Silicene on substrates: a way to preserve or tune its electronic properties, *J. Phys. Chem. C*, 2013, **117**(20), 10353–10359. Available from: **https://pubs.acs.org/doi/10.1021/jp311836m**.

66 T. Li, C. He and W. Zhang, Rational design of porous carbon allotropes as anchoring materials for lithium sulfur batteries, *J. Energy Chem.*, 2021, **52**, 121–129. Available from: **https://www.sciencedirect.com/science/article/pii/S2095495620302813**.

67 Y. Wu, C. He and W. Zhang, Novel Design Strategy of High Activity Electrocatalysts toward Nitrogen Reduction Reaction via Boron, Transition-Metal Hybrid Double-Atom Catalysts, *ACS Appl. Mater. Interfaces*, 2021, **13**(40), 47520–47529, DOI: **10.1021/acsami.1c11889**.

68 Y. Cui, L. Peng, L. Sun, M. Li, X. Zhang and Y. Huang, Structures, stabilities and piezoelectric properties of Janus gallium oxides and chalcogenides monolayers, *J. Phys.: Condens. Matter*, 2019, **32**(8), 08LT01.

69 Y. Mogulkoc, R. Caglayan and Y. O. Ciftci, Band Alignment in Monolayer Boron Phosphide with Janus MoSSe Heterobilayers under Strain and Electric Field, *Phys. Rev. Appl.*, 2021, **16**, 024001. Available from: **https://link.aps.org/doi/10.1103/PhysRevApplied.16.024001**.

70 Z. Deng, Z. Li and W. Wang, Electron affinity and ionization potential of two-dimensional honeycomb sheets: a first principle study, *Chem. Phys. Lett.*, 2015, **637**, 26–31. Available from: **https://www.sciencedirect.com/science/article/pii/S000926141500576X**.

71 B. Radisavljevic, A. Radenovic, J. Brivio, V. Giacometti and A. Kis, Single-layer MoS_2 transistors, *Nat. Nanotechnol.*, 2011, **6**(3), 147–150.

72 J. Tian, A. Katsounaros, D. Smith and Y. Hao, Graphene Field-Effect Transistor Model With Improved Carrier Mobility Analysis, *IEEE Trans. Electron Devices*, 2015, **62**(10), 3433–3440.

73 X. Feng, X. Huang, L. Chen, W. C. Tan, L. Wang and K. W. Ang, High Mobility Anisotropic Black Phosphorus Nanoribbon Field-Effect Transistor, *Adv. Funct. Mater.*, 2018, **28**(28), 1801524. Available from: **https://onlinelibrary.wiley.com/doi/abs/10.1002/adfm.201801524**.

74 S. Das, D. Pandey, J. Thomas and T. Roy, The Role of Graphene and Other 2D Materials in Solar Photovoltaics, *Adv. Mater.*, 2019, **31**(1), 1802722. Available from: **https://onlinelibrary.wiley.com/doi/abs/10.1002/adma.201802722**.

75 W. Lei, S. Zhang, G. Heymann, X. Tang, J. Wen and X. Zheng, *et al.*, A new 2D high-pressure phase of $PdSe_2$ with high-mobility transport anisotropy for photovoltaic applications, *J. Mater. Chem. C*, 2019, **7**, 2096–2105, DOI: **10.1039/C8TC06050A**.

76 W. X. Zhang, Y. Yin and C. P. He, Doping Promotes the Spontaneous Visible-Light-Driven Photocatalytic Water Splitting in Isomorphic Type II GaSe/InS Heterostructure,

 This journal is © the Owner Societies 2022

Published on 05 April 2022. Downloaded by Ankara University on 10/29/2022 10:51:31 AM.

J. Phys. Chem. Lett., 2021, **12**(33), 7892–7900, DOI: **10.1021/acs.jpclett.1c02040**.

77 W. X. Zhang, Y. Yin and C. He, Spontaneous Enhanced Visible-Light-Driven Photocatalytic Water Splitting on Novel Type-II GaSe/CN and Ga_2SSe/CN vdW Heterostructures, *J. Phys. Chem. Lett.*, 2021, **12**(21), 5064–5075, DOI: **10.1021/acs.jpclett.1c01023**.

78 C. He, F. Han and W. Zhang, The InSe/g-CN van der Waals hybrid heterojunction as a photocatalyst for water splitting driven by visible light, *Chin. Chem. Lett.*, 2022, **33**(1), 404–409. Available from: **https://www.sciencedirect.com/science/article/pii/S1001841721005027**.

79 L. Cheng, C. Zhang and Y. Liu, Intrinsic charge carrier mobility of 2D semiconductors, *Comput. Mater. Sci.*, 2021, **194**, 110468. Available from: **https://www.sciencedirect.com/science/article/pii/S0927025621001932**.

80 Y. Cui, L. Peng, L. Sun, Q. Qian and Y. Huang, Two-dimensional few-layer group-III metal monochalcogenides as effective photocatalysts for overall water splitting in the visible range, *J. Mater. Chem. A*, 2018, **6**, 22768–22777, DOI: **10.1039/C8TA08103D**.

81 B. Zhou, S. J. Gong, K. Jiang, L. Xu, L. Shang and J. Zhang, *et al.*, A type-II GaSe/GeS heterobilayer with strain enhanced photovoltaic properties and external electric field effects, *J. Mater. Chem. C*, 2020, **8**, 89–97, DOI: **10.1039/C9TC05840K**.

82 M. M. Obeid, A. Bafekry, S. Ur Rehman and C. V. Nguyen, A type-II GaSe/HfS_2 van der Waals heterostructure as promising photocatalyst with high carrier mobility, *Appl. Surf. Sci.*, 2020, **534**, 147607. Available from: **https://www.sciencedirect.com/science/article/pii/S0169433220323643**.

83 Z. G. Shao, X. S. Ye, L. Yang and C. L. Wang, First-principles calculation of intrinsic carrier mobility of silicene, *J. Appl. Phys.*, 2013, **114**(9), 093712, DOI: **10.1063/1.4820526**.

84 M. Topsakal, H. H. Gürel and S. Ciraci, Effects of charging and electric field on graphene oxide, *J. Phys. Chem. C*, 2013, **117**(11), 5943–5952, DOI: **10.1021/jp310352u**.

85 Y. T. Lee and T. Ozaki, OpenMX Viewer: a web-based crystalline and molecular graphical user interface program, *J. Mol. Graphics Modell.*, 2019, **89**, 192–198, DOI: **10.1016/j.jmgm.2019.03.013**.

86 H. T. T. Nguyen, M. M. Obeid, A. Bafekry, M. Idrees, T. V. Vu and H. V. Phuc, *et al.*, Interfacial characteristics, Schottky contact, and optical performance of a graphene/Ga_2SSe van der Waals heterostructure: Strain engineering and electric field tunability, *Phys. Rev. B: Condens. Matter Mater. Phys.*, 2020, **102**, 075414. Available from: **https://link.aps.org/doi/10.1103/PhysRevB.102.075414**.